

# 1 The Silicon Vertex Detector of the Belle II Experiment

2 Y. Uematsu<sup>a</sup>, K. Adamczyk<sup>t</sup>, L. Aggarwal<sup>l</sup>, H. Aihara<sup>q</sup>, T. Aziz<sup>j</sup>, S. Bacher<sup>t</sup>,  
3 S. Bahinipati<sup>f</sup>, G. Batignani<sup>k,l</sup>, J. Baudot<sup>e</sup>, P. K. Behera<sup>g</sup>, S. Bettarini<sup>k,l</sup>,  
4 T. Bilka<sup>c</sup>, A. Bozek<sup>t</sup>, F. Buchsteiner<sup>b</sup>, G. Casarosa<sup>k,l</sup>, L. Corona<sup>k,l</sup>, T. Czank<sup>p</sup>,  
5 S. B. Das<sup>h</sup>, G. Dujany<sup>e</sup>, C. Finck<sup>e</sup>, F. Forti<sup>k,l</sup>, M. Friedl<sup>b</sup>, A. Gabrielli<sup>m,n</sup>,  
6 E. Ganiev<sup>m,n</sup>, B. Gobbo<sup>n</sup>, S. Halder<sup>j</sup>, K. Hara<sup>r,o</sup>, S. Hazra<sup>j</sup>, T. Higuchi<sup>p</sup>,  
7 C. Irmeler<sup>b</sup>, A. Ishikawa<sup>r,o</sup>, H. B. Jeon<sup>s</sup>, Y. Jin<sup>m,n</sup>, C. Joo<sup>p</sup>, M. Kaleta<sup>t</sup>,  
8 A. B. Kaliyar<sup>j</sup>, J. Kandra<sup>c</sup>, K. H. Kang<sup>s</sup>, P. Kapusta<sup>t</sup>, P. Kodyš<sup>c</sup>, T. Kohriki<sup>r</sup>,  
9 M. Kumar<sup>h</sup>, R. Kumar<sup>i</sup>, C. La Licata<sup>p</sup>, K. Lalwani<sup>h</sup>, R. Le Boucher<sup>d</sup>,  
10 S. C. Lee<sup>s</sup>, J. Libby<sup>g</sup>, L. Martel<sup>e</sup>, L. Massacesi<sup>k,l</sup>, S. N. Mayekar<sup>j</sup>,  
11 G. B. Mohanty<sup>j</sup>, T. Morii<sup>p</sup>, K. R. Nakamura<sup>r,o</sup>, Z. Natkaniec<sup>t</sup>, Y. Onuki<sup>q</sup>,  
12 W. Ostrowicz<sup>t</sup>, A. Paladino<sup>k,l</sup>, E. Paoloni<sup>k,l</sup>, H. Park<sup>s</sup>, G. Polat<sup>d</sup>, K. K. Rao<sup>j</sup>,  
13 I. Ripp-Baudot<sup>e</sup>, G. Rizzo<sup>k,l</sup>, D. Sahoo<sup>j</sup>, C. Schwanda<sup>b</sup>, J. Serrano<sup>d</sup>,  
14 J. Suzuki<sup>r</sup>, S. Tanaka<sup>r,o</sup>, H. Tanigawa<sup>q</sup>, R. Thalmeier<sup>b</sup>, R. Tiwari<sup>j</sup>,  
15 T. Tsuboyama<sup>r,o</sup>, O. Verbycka<sup>t</sup>, L. Vitale<sup>m,n</sup>, K. Wan<sup>q</sup>, Z. Wang<sup>q</sup>, J. Webb<sup>a</sup>,  
16 J. Wiechczynski<sup>l</sup>, H. Yin<sup>b</sup>, L. Zani<sup>d</sup>,

17 (Belle-II SVD Collaboration)

18 <sup>a</sup>*School of Physics, University of Melbourne, Melbourne, Victoria 3010, Australia*

19 <sup>b</sup>*Institute of High Energy Physics, Austrian Academy of Sciences, 1050 Vienna, Austria*

20 <sup>c</sup>*Faculty of Mathematics and Physics, Charles University, 121 16 Prague, Czech Republic*

21 <sup>d</sup>*Aix Marseille Université, CNRS/IN2P3, CPPM, 13288 Marseille, France*

22 <sup>e</sup>*IPHC, UMR 7178, Université de Strasbourg, CNRS, 67037 Strasbourg, France*

23 <sup>f</sup>*Indian Institute of Technology Bhubaneswar, Satya Nagar, India*

24 <sup>g</sup>*Indian Institute of Technology Madras, Chennai 600036, India*

25 <sup>h</sup>*Malaviya National Institute of Technology Jaipur, Jaipur 302017, India*

26 <sup>i</sup>*Punjab Agricultural University, Ludhiana 141004, India*

27 <sup>j</sup>*Tata Institute of Fundamental Research, Mumbai 400005, India*

28 <sup>k</sup>*Dipartimento di Fisica, Università di Pisa, I-56127 Pisa, Italy*

29 <sup>l</sup>*INFN Sezione di Pisa, I-56127 Pisa, Italy*

30 <sup>m</sup>*Dipartimento di Fisica, Università di Trieste, I-34127 Trieste, Italy*

31 <sup>n</sup>*INFN Sezione di Trieste, I-34127 Trieste, Italy*

32 <sup>o</sup>*The Graduate University for Advanced Studies (SOKENDAI), Hayama 240-0193, Japan*

33 <sup>p</sup>*Kavli Institute for the Physics and Mathematics of the Universe (WPI), University of*

34 *Tokyo, Kashiwa 277-8583, Japan*

35 <sup>q</sup>*Department of Physics, University of Tokyo, Tokyo 113-0033, Japan*

36 <sup>r</sup>*High Energy Accelerator Research Organization (KEK), Tsukuba 305-0801, Japan*

37 <sup>s</sup>*Department of Physics, Kyungpook National University, Daegu 41566, Korea*

38 <sup>t</sup>*H. Niewodniczanski Institute of Nuclear Physics, Krakow 31-342, Poland*

---

## 39 Abstract

40 The Silicon Vertex Detector (SVD) is a part of the vertex detector in the  
41 Belle II experiment at the SuperKEKB collider (KEK, Japan). Since the start  
42 of data taking in spring 2019, the SVD has been operating stably and reliably

43 with a high signal-to-noise ratio and hit efficiency, achieving good spatial resolu-  
44 tion and high track reconstruction efficiency. The hit occupancy, which mostly  
45 comes from the beam-related background, is currently about 0.5% in the in-  
46 nermost layer, causing no impact on the SVD performance. In anticipation of  
47 the operation at higher luminosity in the next years, two strategies to sustain  
48 the tracking performance in future high beam background conditions have been  
49 developed and tested on data. One is to reduce the number of signal waveform  
50 samples to decrease dead time, data size, and occupancy. The other is to utilize  
51 the good hit-time resolution to reject the beam background hits. We also mea-  
52 sured the radiation effects on the sensor current, strip noise, and full depletion  
53 voltage caused during the first two and a half years of operation. The results  
54 show no detrimental effect on the SVD performance.

55 *Keywords:* Silicon strip detector, Vertex detector, Tracking detector, Belle II

---

## 56 1. Introduction

57 The Belle II experiment [1] aims to probe new physics beyond the Standard  
58 Model in high-luminosity  $e^+e^-$  collisions at the SuperKEKB collider (KEK,  
59 Japan) [2]. The main collision energy in the center-of-mass system is 10.58 GeV  
60 on the  $\Upsilon(4S)$  resonance, which enables various physics programs based on the  
61 large samples of B mesons,  $\tau$  leptons, and D mesons. Also, the asymmetric  
62 energy of the 7 GeV electron beam and 4 GeV positron beam is adopted for  
63 time-dependent  $CP$  violation measurements. The target of SuperKEKB is to  
64 accumulate an integrated luminosity of  $50 \text{ ab}^{-1}$  with peak luminosity of about  
65  $6 \times 10^{35} \text{ cm}^{-2}\text{s}^{-1}$ . In June 2021, SuperKEKB recorded the world's highest  
66 instantaneous luminosity of  $3.1 \times 10^{34} \text{ cm}^{-2}\text{s}^{-1}$ . The data accumulated before  
67 July 2021 corresponds to an integrated luminosity of  $213 \text{ fb}^{-1}$ .

68 The Vertex Detector (VXD) is the innermost detector in the Belle II detector  
69 system. The VXD has six layers: the inner two layers (layers 1 and 2) are the  
70 Pixel Detector (PXD), and the outer four layers (layers 3 to 6) are the Silicon  
71 Vertex Detector (SVD). The schematic cross-sectional view of the VXD is shown

72 in Fig. 1. The PXD consists of DEPFET pixel sensors, and its innermost radius  
 73 is 1.4 cm from the beam interaction point (IP). A detailed description of the  
 74 SVD appears in Sec. 2.

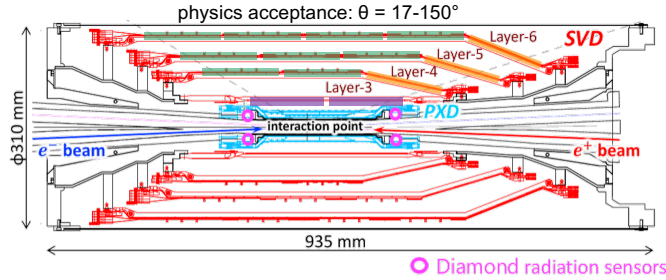


Figure 1: Schematic cross-sectional view of the VXD. The SVD is red, the PXD is light blue, and the IP beam pipe diamonds are pink circles. In the upper half of the VXD the locations of the three types of SVD DSSDs are indicated by boxes in three colors: purple for small sensors, green for large sensors, and orange for trapezoidal sensors as described in Tab. 1.

75 Diamond sensors [3], used to monitor the radiation dose and for the beam  
 76 abort system, are mounted on the IP beam pipe and the bellows pipes outside of  
 77 the VXD. The pink circles in Fig. 1 indicate the locations of the diamond sensors  
 78 on the IP beam pipe. The diamond's measured doses are used to estimate  
 79 the dose in the SVD. The diamond system also sends beam abort requests to  
 80 SuperKEKB if the radiation level gets too high to avoid severe damage to the  
 81 detector.

## 82 2. Belle II Silicon Vertex Detector

83 The SVD is crucial for extrapolating the tracks to the PXD to measure the  
 84 decay vertices with the PXD and point at a region-of-interest limiting the PXD  
 85 readout data volume. Other roles of the SVD are the standalone track recon-  
 86 struction of low-momentum charged particles and their particle identification  
 87 using ionization energy deposits. The SVD also plays a critical role in the decay  
 88 vertex measurement in the case of long-lived particles like  $K_S$  mesons, which  
 89 decay inside the SVD volume.

90 The SVD [4] consists of four layers of double-sided silicon strip detectors  
 91 (DSSDs). The material budget of the SVD is about 0.7% of a radiation length  
 92 per layer. On each DSSD plane, a local coordinate is defined with  $u$  and  $v$ :  
 93  $u$ -axis along n-side strips and  $v$ -axis perpendicular to  $u$ -axis. In other words,  
 94 p-side strips and n-side strips provide  $u$  and  $v$  information, respectively. In the  
 95 cylindrical coordinate,  $u$  corresponds to  $r$ - $\varphi$  information and  $v$  corresponds to  
 96  $z$  information. The SVD consists of three types of sensors: “small” rectangular  
 97 sensors in layer 3, “large” rectangular sensors in the barrel region of layers 4, 5,  
 98 and 6, and “trapezoidal” sensors in the forward region of layers 4, 5, and 6, which  
 99 is slanted. They are indicated by purple, green, and orange boxes in Fig. 1. The  
 100 main characteristics of these three types of sensors are summarized in Tab. 1.  
 101 The sensors are manufactured by two companies: the small and large sensors  
 102 by Hamamatsu and trapezoidal sensors by Micron. The full depletion voltage is  
 103 60 V for Hamamatsu sensors and 20 V for Micron sensors; both types of sensors  
 104 are operated at 100 V. In total, 172 sensors are assembled, corresponding to a  
 105 sensor area of 1.2 m<sup>2</sup> and approximately 224,000 readout strips.

	Small	Large	Trapezoidal
No. of u/p-strips	768	768	768
u/p-strip pitch	50 $\mu\text{m}$	75 $\mu\text{m}$	50–75 $\mu\text{m}$
No. of v/n-strips	768	512	512
v/n-strip pitch	160 $\mu\text{m}$	240 $\mu\text{m}$	240 $\mu\text{m}$
Thickness	320 $\mu\text{m}$	320 $\mu\text{m}$	300 $\mu\text{m}$
Manufacturer	Hamamatsu		Micron

Table 1: Table of the main characteristics of the three types of sensors. Only readout strips are taken into account for number of strips and strip pitch. All sensors have one intermediate floating strip between two readout strips.

106 Sensor strips are AC coupled to the front-end ASIC, the APV25 [5], which  
 107 was originally developed for the CMS Silicon Tracker. The APV25 tolerates  
 108 more than 100 Mrad of radiation. It has 128 channels with a shaping time of  
 109 about 50 ns. For the SVD, the APV25 is operated in “multi-peak” mode. The

110 mechanism of the data sampling in the multi-peak mode is explained in Fig. 2.  
111 The chip samples the height of the signal waveform with the 32 MHz clock (31 ns  
112 period) and stores each sample's information in an analog ring buffer. Since  
113 the bunch-crossing frequency is eight times faster than the sampling clock, the  
114 stored samples are not synchronous to the beam collision, in contrast to CMS,  
115 which motivates operation in the multi-peak mode. In the present readout  
116 configuration (the six-samples mode), at every reception of the Belle II global  
117 Level-1 trigger, the chip reads out six successive samples of the signal waveform  
118 stored in the buffers. The six-samples mode offers a wide enough time window  
119 ( $6 \times 31 \text{ ns} = 187 \text{ ns}$ ) to accommodate large timing shifts of the trigger. In  
120 preparation for operation with higher luminosity, where background occupancy,  
121 trigger dead-time, and the data size increase, we developed the three/six-mixed  
122 acquisition mode (mixed-mode). The mixed-mode is a new method to read  
123 out the signal samples from the APV25, in which the number of the samples  
124 changes between three and six in each event, depending on the timing precision  
125 of each Level-1 trigger signal in that event. For triggers with precise timing,  
126 three-samples data are read out and the data have half time window and half  
127 data size compared to ones of six-samples data, resulting in the reduction of the  
128 effects due to higher luminosity. This functionality was already implemented  
129 in the running system and confirmed by a few hours of smooth physics data  
130 taking. Before we start to use the mixed-mode, the effect on the performance  
131 due to the change of the acquisition mode is to be assessed. As the first step,  
132 the effect in the hit efficiency was evaluated as described in Sec. 3.

133 The APV25 chips are mounted on each middle sensor (chip-on-sensor con-  
134 cept) with thermal isolation foam in between. The merit of this concept is  
135 shorter signal propagation length, leading to smaller capacitance of the signal  
136 line and hence reduced noise level. To minimize the material budget the APV25  
137 chips on the sensor are thinned down to 100  $\mu\text{m}$ . The APV25 chips are mounted  
138 on a single side of the sensor and readout of the signals from the opposite side is  
139 performed via wrapped flexible printed circuits. The power consumption of the  
140 APV25 chip is 0.4 W/chip and 700 W in the entire SVD. The chips are cooled

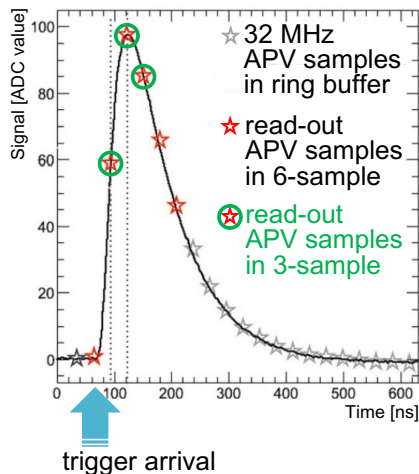


Figure 2: Example of sampling in “multi-peak” mode of the APV25. The black line shows the signal waveform after the CR-RC shaper circuit. The stars show the sampled signal height recorded in the analog ring buffer according to the 32 MHz sampling clock. The red stars indicate the six successive samples read out at the trigger reception in the six-samples mode. The red stars with a green circle indicate the samples read out in the three-samples acquisition.

141 by a bi-phase  $-20^{\circ}\text{C}$   $\text{CO}_2$  evaporative cooling system.

### 142 3. Performance

143 Since March 2019, the SVD has been operating reliably and smoothly for  
 144 two and a half years. The total fraction of masked strips is about 1%. There  
 145 was only one issue where one APV25 chip (out of 1,748 chips) was disabled  
 146 during the spring of 2019, which was remediated by reconnecting a cable in the  
 147 summer of 2019.

148 The SVD has also demonstrated stable and excellent performance [6]. The  
 149 hit efficiency is continuously over 99% in most of the sensors. The cluster  
 150 charge distributions are also reasonable. On the u/p-side, the most probable  
 151 values agree with the calculated charge amount induced by MIPs within the  
 152 uncertainty in calibration. On the v/n-side, 10-30% of the collected charge is  
 153 lost compared to the signal collected on the u/p-side, due to the presence of the

154 floating strip combined with the large pitch on the v/n-side. The most probable  
 155 values of the cluster signal-to-noise ratio distributions range from 13 to 30.

156 We measured the cluster position resolution by analyzing the  $e^+e^- \rightarrow \mu^+\mu^-$   
 157 data [7]. The resolution is estimated from the residual between the cluster po-  
 158 sition and the track position, not biased by the target cluster, after subtracting  
 159 the effect of the track extrapolation error. The cluster position resolutions for  
 160 different incident angles are shown in Fig. 3. The observed resolution has the  
 161 expected shape, showing a minimum at the incident angle for which the projec-  
 162 tion of the track along the direction perpendicular to the strips on the detector  
 163 plane corresponds to two strip pitches. Given the various sensor pitches with  
 164 one floating strip, the minimum is expected at 14 (21) degrees on the v/n-side  
 165 and at 4 (7) degrees on the u/p-side, respectively for layer 3 (4, 5, and 6). The  
 166 resolution for normal incident angle is also in good agreement with the expected  
 167 digital resolution, that is 23 (35)  $\mu\text{m}$  on the v/n-side, 7 (11)  $\mu\text{m}$  on the u/p-side,  
 168 respectively for layer 3 (4, 5, and 6). Still, some studies are ongoing to improve  
 169 the resolution especially for the layer-3 u/p-side, where at normal incidence a  
 170 slightly higher resolution is measured (9  $\mu\text{m}$ ) compared to the expectations.

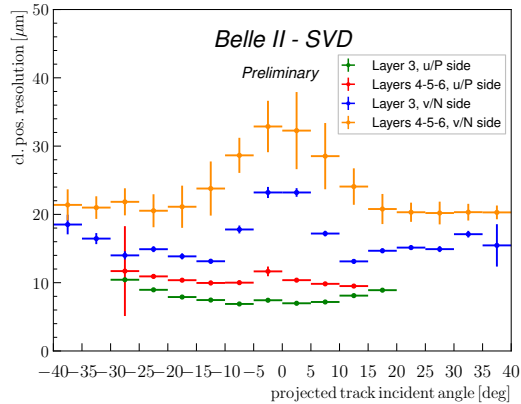


Figure 3: The SVD cluster position resolution depending on the projected track incident angle. The green (blue) plot shows the resolution in the u/p-side (n/v-side) of layer-3 sensors, and the red (yellow) one shows the u/p-side (n/v-side) of layers-4, 5, and 6 sensors.

171 The cluster hit-time resolution was also evaluated in candidate hadronic

172 events<sup>1</sup> using the reference event time estimated by the Central Drift Chamber  
 173 (CDC) outside of the SVD. The error on the event time, about 0.7 ns, was  
 174 subtracted to evaluate the intrinsic SVD hit-time resolution. The resulting  
 175 resolution is 2.9 ns on the u/p-side and 2.4 ns on the v/n-side. With such  
 176 precise hit-time information, it is possible to reject off-time background hits  
 177 efficiently. The hit-time distributions for signal<sup>2</sup> and background<sup>3</sup> are shown  
 178 in Fig. 4. The signal distribution has a narrow peak, while the background  
 179 hit-time distribution is broad and almost flat in the signal peak region. The  
 180 separation power of the hit-time is high, as expected. For example, if we reject  
 181 hits with the hit-time less than  $-38$  ns in this plot, we can reject 45% of the  
 182 background hits while keeping 99% of the signal hits. The background rejection  
 183 based on the hit-time is essential to sustain the good tracking performance in  
 184 the future high beam background condition.

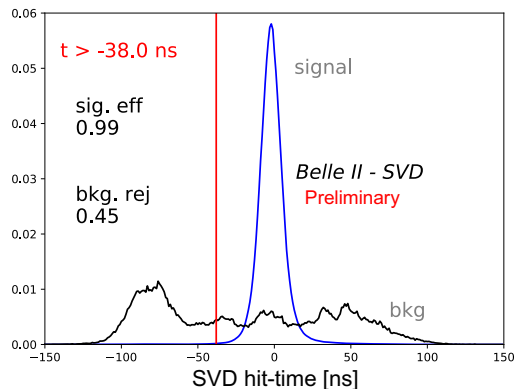


Figure 4: Example of the background hit rejection using hit-time. The blue distribution shows the signal, and the black distribution shows the background. Assuming the hit-time cut at  $-38$  ns, the signal hit efficiency of 99% and the background hit rejection of 45% are achieved.

185 The performance in three-samples data was compared with that in six-  
 186 samples data to evaluate the performance in the mixed-mode. If the trigger

---

<sup>1</sup>The events with more than three good tracks and not like Bhabha scattering.

<sup>2</sup>The clusters found to be used in the tracks in the hadronic events.

<sup>3</sup>The clusters in events triggered by delayed-Bhabha pseudo-random trigger.



187 timing has no deviation, the three-samples data will show comparable perfor-  
 188 mance to the six-samples data because the relevant part of the signal waveform  
 189 to evaluate the necessary signal properties, i.e., the signal height and the sig-  
 190 nal timing can be accommodated in the three-sample's time window. However,  
 191 when the trigger has a jitter and the timing shift happens, some part of the  
 192 signal waveform can be out of the three-sample's time window, and the recon-  
 193 struction performance deteriorates. We examined the effect on the hit efficiency  
 194 as a function of the trigger timing shift. The effect is evaluated by the rel-  
 195 ative hit efficiency, which is defined as the ratio of the hit efficiency in the  
 196 three-samples data to the one in the six-samples data. For this study, the three-  
 197 samples data are emulated in the offline analysis from the six-samples data by  
 198 selecting consecutive three samples at a fixed latency with respect to the Level-  
 199 1 trigger signal. The trigger timing shift is evaluated by the CDC event time.  
 200 The resulting relative efficiencies as a function of the trigger timing shift in the  
 201 hadronic events are shown in Fig. 5. The decreasing trend is observed for the  
 202 shift of the trigger timing, as expected. As a result, the relative efficiency is  
 203 over 99.9% for the trigger timing shift within  $\pm 30$  ns, which is almost all the  
 204 events.

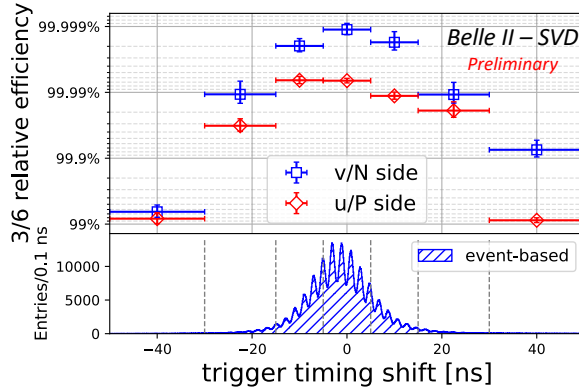


Figure 5: The relative hit efficiencies (the ratios of the hit efficiency in the three-samples data to the one in the six-samples data) as a function of the trigger timing shift for v/n-side (blue square) and u/p-side (red diamond). The positive (negative) trigger timing shift corresponds to early (late) trigger timing.

#### 205 4. Beam-related background effects on SVD

206 The beam-related background (BG) increases the hit occupancy of the SVD,  
207 which in turn degrades the tracking performance. Considering this performance  
208 degradation, we set the occupancy limit in layer-3 sensors to be about 3%, which  
209 will be loosened roughly by a factor of two after we apply the hit-time rejection  
210 described in Sec. 3. With the current luminosity, the average hit occupancy  
211 in layer-3 sensors is below 0.5%. However, the projection of the hit occupancy  
212 at the luminosity of  $8 \times 10^{35} \text{ cm}^{-2}\text{s}^{-1}$  is about 3% in layer-3 sensors. The  
213 projected occupancy comes from the Monte Carlo (MC) simulation scaled by  
214 the data/MC ratio determined from the BG data of the current beam optics.  
215 The corresponding integrated dose, using the data/MC-rescaled BG extrapo-  
216 lation, is about 0.2 Mrad/smy, and the equivalent 1-MeV neutron fluence is  
217 about  $5 \times 10^{11} \text{ neq/cm}^2/\text{smy}$  (smy: Snowmass Year =  $10^7$  sec). Considering the  
218 radiation hardness of the SVD sensors, about 10 Mrad and about  $10^{13} \text{ neq/cm}^2$ ,  
219 based on the experience of similar DSSD sensors used in the BaBar Silicon Ver-  
220 tex Tracker [8], we expect to be able to safely operate the SVD even for ten  
221 years at high luminosity, with safety margin of factor two to three against BG  
222 extrapolation. The long-term BG extrapolation is affected by large uncertain-  
223 ties from the optimization of collimator settings in MC and the future evolution  
224 of the beam injection background, which is not simulated. This uncertainty,  
225 together with the relatively small safety factor of two to three between the BG  
226 extrapolation and the detector limits, motivates the VXD upgrade to improve  
227 the tolerance of the hit rates and the radiation damage, and the technology  
228 assessment is ongoing for multiple sensor options.

229 In the first two and a half years of operation, the integrated dose in the  
230 layer-3 mid-plane sensors, which are the most exposed in the SVD, is esti-  
231 mated to be 70 krad. The estimation is based on the measured dose by the  
232 diamonds on the beam pipe exploiting the measured correlation between the  
233 SVD occupancy and the diamond dose [9]. Thanks to a new random trigger  
234 line recently introduced, we improved the dose analysis, removing an overes-

235 timation of about factor three in the previous study. The new estimate still  
236 has an uncertainty of about 50% mainly due to the unavailability of this newly  
237 introduced trigger before December 2020. Assuming the dose/ $n_{\text{eq}}$  fluence ra-  
238 tio of  $2.3 \times 10^9$   $n_{\text{eq}}/\text{cm}^2/\text{krad}$  from MC, 1-MeV equivalent neutron fluence is  
239 evaluated to be about  $1.6 \times 10^{11}$   $n_{\text{eq}}/\text{cm}^2$ .

240 The effect of the integrated dose on the sensor leakage current is measured,  
241 and the results show a clear linear correlation as in the upper plot of Fig. 6. The  
242 slopes for all the sensors are 2–5  $\mu\text{A}/\text{cm}^2/\text{Mrad}$ , as summarized in the lower  
243 plot of Fig. 6. The large variations can be explained by temperature effects and  
244 the deviation of sensor-by-sensor dose from the average in each layer used in  
245 the estimation. The slopes are in the same order of magnitude as previously  
246 measured in the BaBar experiment [8], 1  $\mu\text{A}/\text{cm}^2/\text{Mrad}$  at 20°C. The precise  
247 temperature in layer 3 of the SVD is unknown but expected to be in a similar  
248 regime. While the leakage current is increasing, the impact on the strip noise  
249 is suppressed by the short shaping time (50 ns) in APV25. It is expected to be  
250 comparable to the strip-capacitive noise only after 10 Mrad irradiation and not  
251 problematic for ten years where the integrated dose is estimated to be 2 Mrad.

252 The evolution of the noise with the integrated dose is shown in Fig. 7. The  
253 noise increase of 20–25% is observed in layer 3, but this does not affect the  
254 SVD performance. This noise increase is likely due to the radiation effects on  
255 the sensor surface. Fixed oxide charges on sensor surface increase with dose,  
256 with some saturation expected at around 100 krad, enlarging also non-linearly  
257 the inter-strip capacitance, also expected to saturate with dose. The noise  
258 saturation is already observed on the v/n-side and also starts to be seen on the  
259 u/p-side.

260 The full depletion voltage of the sensor is also a key property that can be  
261 affected by the radiation damage. It can be measured from the v/n-side strip  
262 noise, which suddenly decreases at the full depletion voltage because the sensor  
263 substrate is n-type and thus the v/n-side strips are only fully isolated at full  
264 depletion. From this measurement full depletion voltages consistent with mea-  
265 surements performed on the bare sensors before the installation were obtained,

266 ranging from 20 to 60 V, and so far no change in full depletion voltage is ob-  
267 served in the first two and a half years of operation, which is consistent with  
268 the expectation from low integrated neutron fluence of  $1.6 \times 10^{11}$  n<sub>eq</sub>/cm<sup>2</sup>.

## 269 **5. Conclusions**

270 The SVD has been taking data in Belle II since March 2019 smoothly and  
271 reliably. The detector performance is excellent and agrees with expectations.  
272 We are ready to cope with the increased background during higher luminosity  
273 running by rejecting the off-time background hits using hit-time and operating  
274 in the three/six-mixed acquisition mode. In the recent study, the efficiency  
275 loss in the three-samples data is confirmed to be less than 0.1% for the trigger  
276 timing shift within  $\pm 30$  ns. The observed first effects of radiation damage are  
277 also within expectation and do not affect the detector performance.

## 278 **Acknowledgments**

279 This project has received funding from the European Union’s Horizon 2020  
280 research and innovation programme under the Marie Skłodowska-Curie grant  
281 agreements No 644294 and 822070. This work is supported by MEXT, WPI,  
282 and JSPS (Japan); ARC (Australia); BMBWF (Austria); MSMT (Czechia);  
283 CNRS/IN2P3 (France); AIDA-2020 (Germany); DAE and DST (India); INFN  
284 (Italy); NRF and RSRI (Korea); and MNiSW (Poland).

## 285 **References**

- 286 [1] T. Abe, et al., Belle II Technical Design Report (2010). arXiv:1011.0352.
- 287 [2] Y. Ohnishi, et al., Accelerator design at SuperKEKB, Prog. Theor. Exp.  
288 Phys. 2013 (3), 03A011 (03 2013).
- 289 [3] S. Bacher, et al., Performance of the diamond-based beam-loss monitor sys-  
290 tem of Belle II, Nucl. Instrum. Methods Phys. Res., Sect. A 997 (2021)  
291 165157. arXiv:2102.04800.

- 292 [4] K. Adamczyk, et al., The Belle II silicon vertex detector assembly and me-  
293 chanics, Nucl. Instrum. Methods Phys. Res., Sect. A 845 (2017) 38–42, pro-  
294 ceedings of the Vienna Conference on Instrumentation 2016.
- 295 [5] M. J. French, et al., Design and results from the APV25, a deep sub-micron  
296 CMOS front-end chip for the CMS tracker, Nucl. Instrum. Methods Phys.  
297 Res., Sect. A 466 (2001) 359–365.
- 298 [6] G. Rizzo, et al., The Belle II Silicon Vertex Detector: Performance and  
299 Operational Experience in the First Year of Data Taking, JPS Conf. Proc.  
300 34 (2021) 010003.
- 301 [7] R. L. Boucher, et al., Measurement of the cluster position resolution of the  
302 Belle II Silicon Vertex Detector, these NIMA Conference Proceedings.
- 303 [8] B. Aubert, et al., The BaBar detector: Upgrades, operation and perfor-  
304 mance, Nucl. Instrum. Methods Phys. Res., Sect. A 729 (2013) 615–701.
- 305 [9] L. Massaccesi, Performance study of the SVD detector of Belle II and future  
306 upgrades, master thesis, Dipartimento di Fisica *E. Fermi*, Università di Pisa  
307 (2021).  
308 URL <https://docs.belle2.org/record/2759/>

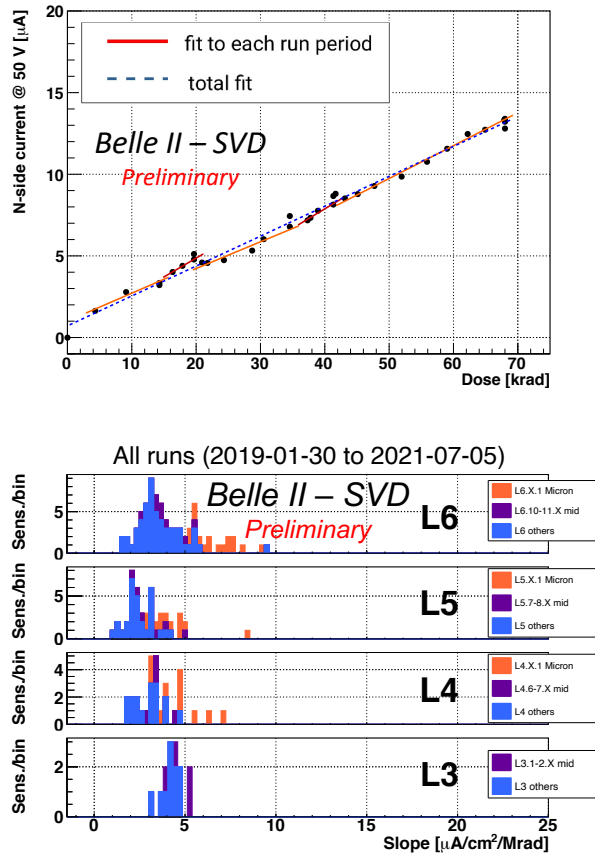


Figure 6: (upper) Effect of the integrated dose on the leakage current in the n/v-side of one layer-3 sensor. The slope is fitted for each run period (solid red line) and all the runs (dashed blue line). Both fit results agree with each other and are consistent with the linear increase. (lower) The fit results of all the sensors for all runs. The sensors are classified as trapezoidal sensors in the forward region (Micron), sensors around the midplane, and the others.

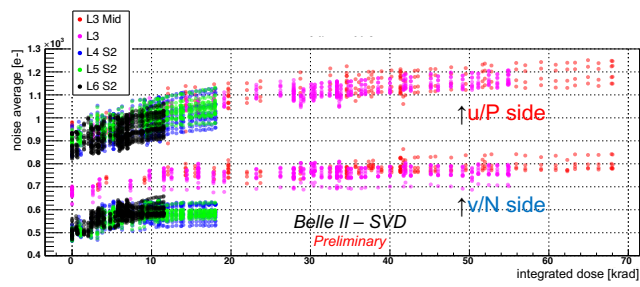


Figure 7: Effect of the integrated dose on the noise average in electron. The upper (lower) series shows the u/p-side (v/n-side) results, respectively.